Materials Today Bio 31 (2025) 101481

Contents lists available at ScienceDirect

Materials Today Bio

journal homepage: www.journals.elsevier.com/materials-today-bio

pH-responsive molybdenum disulphide composite nanomaterials for skin wound healing using "ROS leveraging" synergistic immunomodulation

Zhen Yang [a,b,1], Jiaqian You [c,1], Shaobo Zhai [a], Jing Zhou [a], Sezhen Quni [a], Manxuan Liu [a], Lu Zhang [a], Rui Ma [a], Qiuyue Qin [a], Huimin Huangfu [a], Yidi Zhang [a,**], Yanmin Zhou [a,*]

[a] Jilin Provincial Key Laboratory of Tooth Development and Bone Remodeling, Hospital of Stomatology, Jilin University, Changchun, 130021, Jilin, China
[b] No. 10 East Zangda Road, Chengguan District, Tibet University, Lhasa, 850000, Tibet Autonomous Region, China
[c] Hospital of Stomatology, Guanghua School of Stomatology, Sun Yat-sen University and Guangdong Provincial Key Laboratory of Stomatology, No.56, Lingyuan West Road, Yuexiu District, Guangzhou, 510055, China

ARTICLE INFO

Keywords:
Molybdenum disulfide
Antibacterial
Bimetallic
Polydopamine

ABSTRACT

With the increasing prevalence of drug-resistant bacterial infections, wound bacterial infections have evolved into an escalating medical problem that poses a threat to the individual health as well as global public health. Traditional drug therapy not only suffers from a single treatment method, low drug utilisation and limited therapeutic effect, but long-term antibiotic abuse has significantly increased bacterial resistance. It is imperative to develop an antibiotic-free biomaterial with antibacterial and anti-inflammatory properties. The current use of photothermal therapy (PTT) and photodynamic therapy (PDT) relies on the generation of massive reactive oxygen species (ROS), which inevitably aggravates the inflammatory response. Herein, we developed AuAg bimetallic nanoparticles based on PDA modification and prepared a novel MoS_2-based composite nanomaterials (AuAg@PDA-MoS_2 NPs) with multiple mechanisms of antibacterial and anti-inflammatory potentials through the adhesion of PDA. In the early phase, PDT and PTT generated a large amount of ROS for rapid sterilisation. While in the later stage, MoS_2 mimicked the peroxidase activity to leverage the ROS, balancing the generation of ROS in the infected environment to achieve the long-term anti-inflammatory. *In vitro* experiments showed that the killing efficiency of AuAg@PDA-MoS_2 NPs was nearly 99 % under the irradiation of 808 nm near-infrared light for 10 min, which demonstrated excellent antibacterial activity. *In vivo* experiments showed that 808 nm NIR-assisted AuAg@PDA-MoS_2 NPs to effectively inhibit infection, alleviated the inflammation, and accelerated the wound healing process. Therefore, AuAg@PDA-MoS_2 NPs as a novel biomaterial could achieve programmed antimicrobial and anti-inflammatory effects, which has a promising potential for future application in the treatment of infected wounds.

1. Introduction

As the largest multi-layered organ of the human body, the skin is the first barrier against foreign pathogens and guards human health at all times [1,2]. When this barrier is disrupted, microorganisms at the wound can cause inflammation and the risk of wound infection, impeding the wound healing process [3–5]. Bacterial infections are currently reported to cause approximately 700,000 deaths per year globally and are projected to cause more than 10 million deaths per year by 2050 [6]. Reducing the probability of wound infection is critical to promote wound tissue recovery and has become one of the topical issues in wound therapy worldwide (see Scheme 1).

Photothermal therapy (PTT) can combat bacterial infections by photothermal agent (PTA) to rupture bacterial membranes and denature proteins causing permanent damage through the heat generated by exposure to NIR [7–11]. However, high body temperatures lead to tissue

* Corresponding author. Jilin Provincial Key Laboratory of Tooth Development and Bone Remodeling, Hospital of Stomatology, Jilin University, Changchun, 130021, Jilin, China.
** Corresponding author. Jilin Provincial Key Laboratory of Tooth Development and Bone Remodeling, Hospital of Stomatology, Jilin University, Changchun, 130021, Jilin, China.
E-mail addresses: zhangyd66@jlu.edu.cn (Y. Zhang), zhouym@jlu.edu.cn (Y. Zhou).
[1] Z.Y. and J.Y. contributed equally to this work.

https://doi.org/10.1016/j.mtbio.2025.101481
Received 19 September 2024; Received in revised form 25 December 2024; Accepted 10 January 2025
Available online 10 January 2025

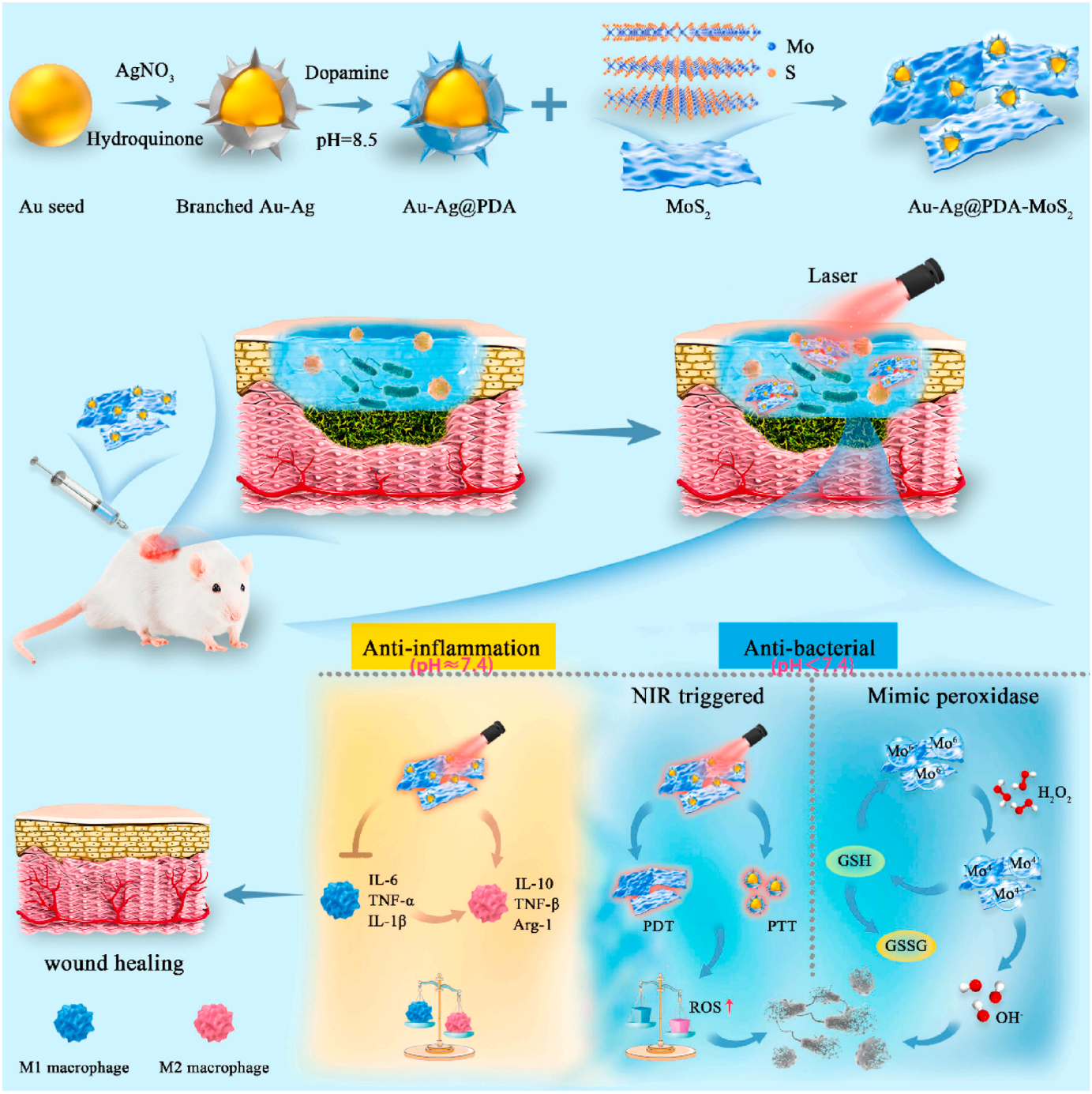

Scheme 1. Schematic representation of the design strategy and mechanism of AuAg@PDA-MoS_2 NPs to promote wound healing.

damage, (up-regulated)the Heat shock proteins (HSPs) making PTT challenging to use in antibacterial applications [12–15]. HSPs are a group of stress-responsive proteins that are widely found in organisms ranging from bacteria to mammals. Studies have shown that when organisms are exposed to high temperatures, HSPs are induced to be expressed in order to protect cells from heat-induced damage [16–18]. The high expression of HSPs within bacteria induced by PTT increases the resistance of bacteria to high temperatures, which weakens the antimicrobial effect of PTT. Antimicrobial photodynamic therapy Photodynamic therapy (PDT) is considered a promising antimicrobial method employing photosensitiser (PS) to generate reactive oxygen species (ROS), which causes oxidative damage to surrounding bacteria. However, the ROS has a shorter penetration distance, which limited the application of PDT in antibacterial field [19]. Thermal therapy with PTT interferes with the structure of the bacterial membrane and facilitates the penetration of ROS generated by PDT over a wider area, whereas the ROS from PDT oxidises HSPs and reduces the therapeutic temperature of the PTT in order to avoid tissue damage [20]. Hence, the integration of PDT and PTT into a single antimicrobial biomaterial produces a more effective antimicrobial effect than a single therapy [21,22].

ROS produced by PDT is a double-edged sword, ROS penetrates bacterial biofilms leading to irreversible damage to proteins and nucleic acids, which plays a crucial role in bacterial eradication [23–25]. However, it is not well known that the excess ROS produced by PS can induce an intense inflammatory response and impede wound healing. Therefore, it is necessary to design a biomaterial capable of balancing

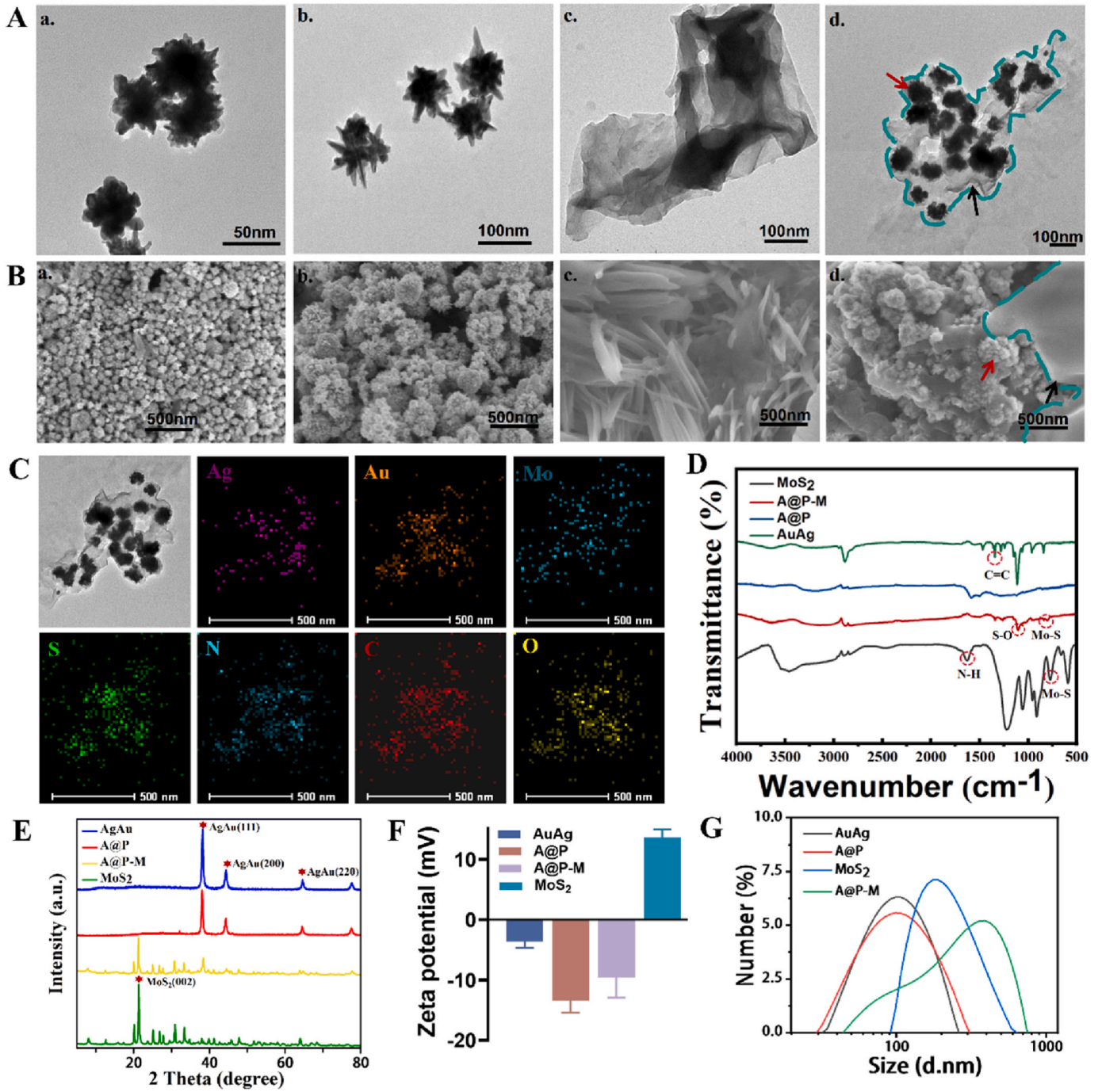

Fig. 1. (A) TEM images of a) AuAg NPs b) A@P NPs c) MoS_2 nanosheets d) A@P-M NPs (the lamellar structure of MoS_2 with dashed lines). (B)SEM images of a) AuAg NPs b) A@P NPs c) MoS_2 nanosheets d) A@P-M NPs (the lamellar structure of MoS_2 with dashed lines). (C) Elemental mapping images of A@P-M NPs. (D) FTIR spectra of AuAg, A@P and A@P-M NPs. (E) XRD patterns of AuAg, A@P and A@P-M NPs. (F). Zeta potentials of the AuAg, A@P, A@P-M NPs and MoS_2 measured by DLS. (G) Hydrodynamic sizes of the AuAg, A@P, A@P-M NPs and MoS_2 measured by DLS.

environmental ROS levels to "leverage" the balance between oxidative and antioxidant processes, which can be utilised to kill bacteria early in the course of an infection, and remove ROS to astringe inflammation after the infection has been cleared [26].

In the past decades, two-dimensional materials such as transition metal-dichalcogenides (TMDs) and their derivatives have shown higher ROS scavenging activity due to their remarkable surface area-to-volume ratio, excellent electron transfer capability, abundant edge/defect sites and electrophilic basal planes through radical conjugation, electron transfer from the edge/defect sites, and hydrogen trapping processes [27,28]. In particular, the transition metal sulfur compound MoS_2 is not only an ideal PS for PDT, but also possesses the ability to mimic the activity of peroxidase (POD), which can converts H_2O_2 into free radicals in the acidic environment during the early stage of bacterial infection which binds to bacterial cell proteins, lipids, and polysaccharides and causes bacterial membrane perforation and death [29–31]. More specifically, Mo^{4+} in MoS_2 has POD-like activity and reacts with endogenous H_2O_2 to produce •OH and Mo^{6+}; while Mo^{6+} has the ability to oxidize glutathione (GSH), which can be reduced to Mo^{4+}, and this cycle of Mo^{4+} and Mo^{6+} ultimately induces a large amount of •OH in bacteria,

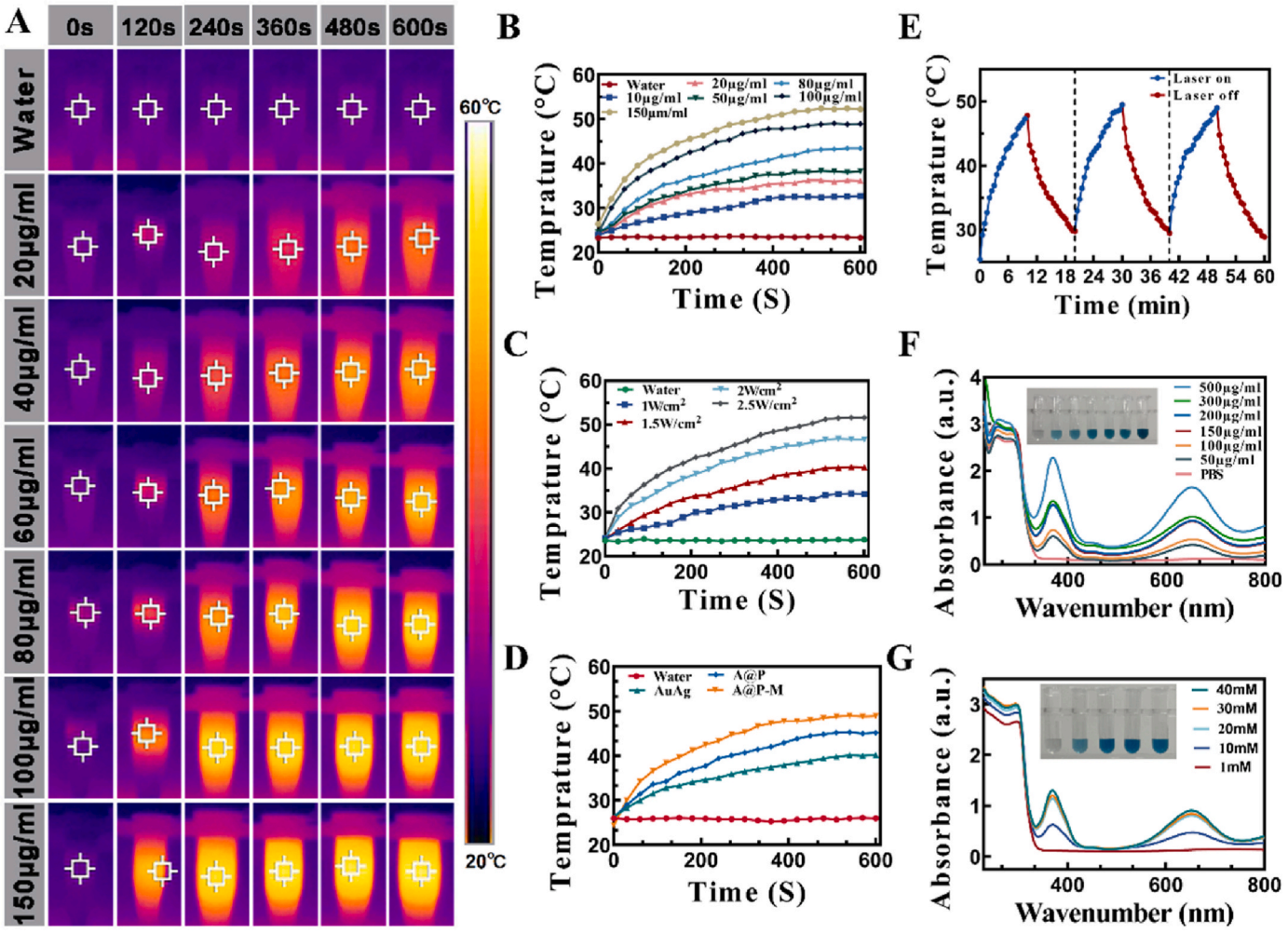

Fig. 2. (A) Thermal images of A@P-M NPs solution (100 μg/mL) under irradiation for 808 nm 10 min at 2 W/cm^2. (B) Photothermal effect of A@P-M with different concentrations (2W/cm^2). (C) Photothermal effect of A@P-M irradiated with different powers of NIR (100 μg/ml). (D) Photothermal effect of different materials under 808 nm NIR irradiation (2W/cm^2). (E) Photostability of A@P-M with 3 cycles under 808 nm irradiation (100 μg/mL). (F) Absorbance spectra of oxTMB under different concentrations of A@P-M (10 mM H_2O_2, 10 mM TMB). (G) Absorbance spectra of ox-TMB under different concentrations of H_2O_2 (100 μg/ml A@P-M, 10 mM TMB).

which can constitute an excellent antimicrobial platform [32–35]. Compared to other 2D materials, the ultra-thin atomic layer structure and the formation of Mo^{6+}/Mo^{4+} redox couple of MoS_2, which can switch between each state in a $Mo^{6+} \leftrightarrow Mo^{4+}$ recycle process, provide a faster conversion of H_2O_2 into •OH [34,36]. What's more, as the bacterial population decreases, the tissue microenvironment gradually returns to the normal physiological state (pH ≈ 7.4), at which time MoS_2 could transfer electrons to scavenge ROS, thus actively inducing the overloading of the pro-inflammatory microenvironment to anti-inflammatory one, showing great anti-inflammatory potential [36]. Thus, MoS_2 can leverage the balance between ROS generation and scavenging by dynamically regulating the immune microenvironment. Furthermore, the large specific surface area and easy surface modification of MoS_2 allow it to better adhere to the bacterial membrane and interact strongly with the bacterial membrane. The cell membrane is an essential component of all bacteria, where the sharp edges of MoS_2 nanosheets can lead to the extraction of the phospholipid bilayer and degradation of the inner and outer cell membranes upon direct physical contact, disrupting the integrity of the cell wall, leading to the leakage of intracellular components and ultimately killing the bacteria [37–39]. The two-dimensional MoS_2 nanosheets have the advantage of "small amount and high efficiency", thus reducing unwanted side effects to a certain extent.

In this study, we synthesised a novel nanohybrid composite (AuAg@PDA-MoS_2), which could enhance the activity of surface-enhanced Raman scattering using branched AuAg nanostructures and provide excellent photo-thermal properties to achieve the PTT. In addition, inspired by the structure of adhesion proteins secreted by mussels, we wrapped PDA and MoS_2 on the surface of (AuAg) bimetallic nanoparticles to form nanocomposites with core-shell structure [40–43]. The introduction of PDA improved the poor stability of AuAg bimetallic nanoparticles and enhanced the PTT effect. The balanced regulation of ROS during the healing process of infected wounds was achieved by the "leveraging" of MoS_2 mimicking peroxidase activity. The results suggest that AuAg@PDA-MoS_2 nanohybrid composites can not only effectively combat bacteria in the early stage of wound healing, but also promote faster healing of skin wounds by inducing the polarisation of M2-phenotyped macrophages and regulating the ROS content in the microenvironment, achieving the transition from a pro-inflammatory to an anti-inflammatory microenvironment. Therefore, AuAg@PDA-MoS_2 achieved an effective combination of PTT and PDT as well as a significant potential as a biomaterial with programmable antimicrobial and anti-inflammatory properties in the field of healing infected wounds.

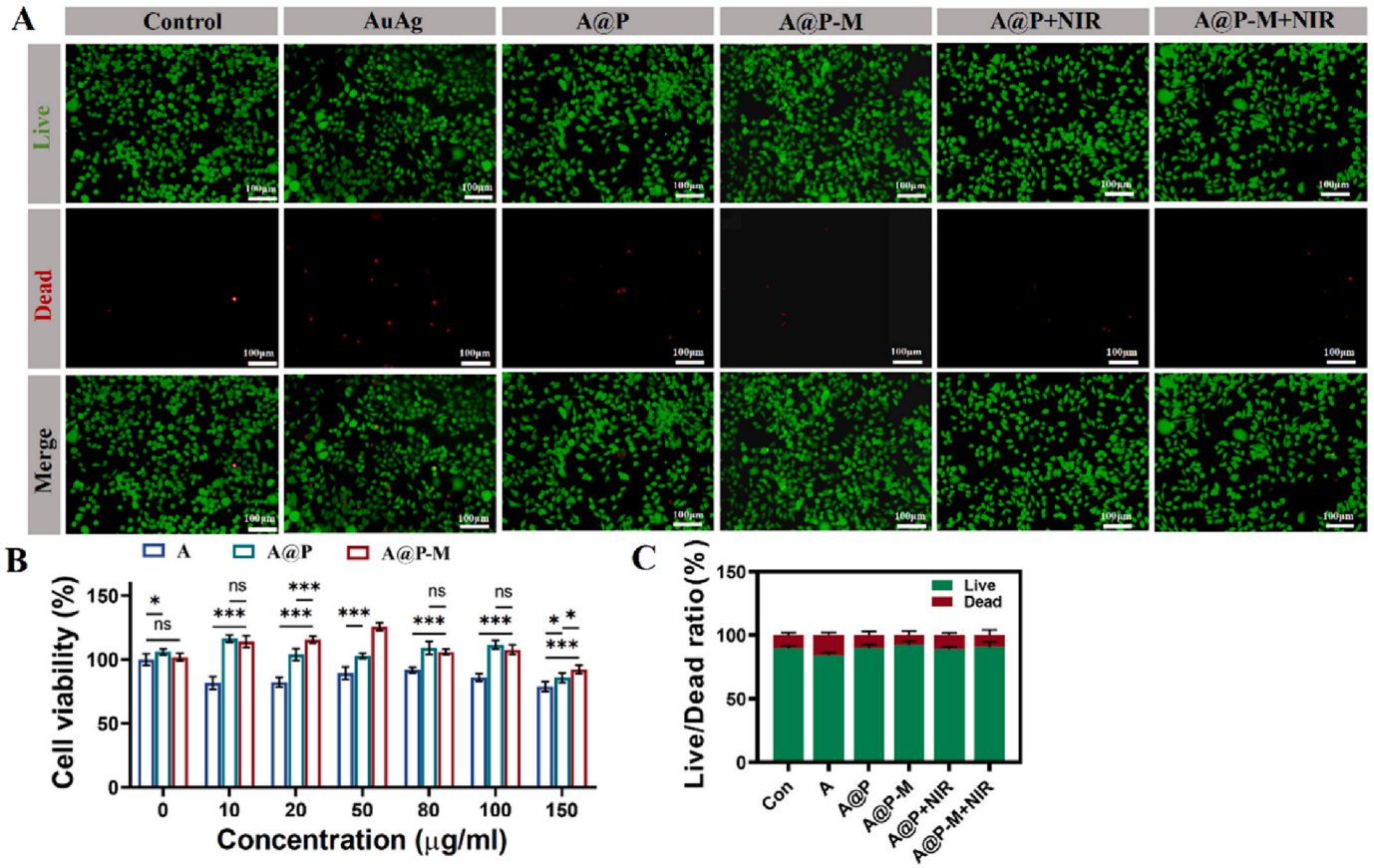

Fig. 3. (A) Calcein AM (green) and PI (red) fluorescence images of L929. (B) The activity of L929 determined by the CCK-8. (C) Quantitative analysis of live-dead staining of cells. (For interpretation of the references to color in this figure legend, the reader is referred to the Web version of this article.)

2. Results

2.1. Characterization of AuAg, A@P and A@P-M NPs

The physical morphology of AuAg, AuAg@PDA (labeled as A@P) and AuAg@PDA-MoS_2 (labeled as A@P-M) NPs was detected by transmission electron microscopy (TEM) and scanning electron microscopy (SEM). The results showed that the AuAg NPs were branch-like with diameters of about 50–60 nm (Fig. 1A/a and 1B/a). The diameter of A@P NPs increases to 90–100 nm due to the PDA shell wrapped around the surface of AuAg NPs (Fig. 1A/b and 1B/b). MoS_2 nanosheets with diameters ranging from 1μm to 3μm, with some overlapping layers existing and elongated spiny protrusions shown in Fig. 1A/c and 1B/c. The A@P NPs (Red arrow) are loaded on the MoS_2 nanosheets (Black arrow) due to the π-π conjugation between the surface PDA and the nanosheets, which results in the formation of a "sheet-loaded sphere structure" by loading the A@P NPs into the nanosheets (in Fig. 1A/d and 1B/d). The HAADF–STEM–EDS mapping elemental analysis images showed that in addition to Au and Ag, Mo and S elements were also observed to be uniformly distributed (Fig. 1C) and the corresponding semi-quantitative analysis also demonstrates the presence of Au, Ag, Mo and S elements in A@P-M (Fig. S2). The XRD spectra of A@P-M NPs exhibit special peaks at 38.2°, 44.4°, and 64.6°, which correspond to (111), (200), and (220), respectively, located on the crystal planes of branched AuAg NPs (Fig. 1E). The 2θ angle of the diffraction peak of MoS_2 (002) crystalline surface fluctuates from 14° to 20° depending on the method of preparation.The XRD results of A@P-M show a special peak of MoS_2 (002) around 20°, which proves that the nanoparticles are successfully loaded on the MoS_2 nanosheets [44,45]. These spectral images match the Joint Committee on Powder Diffraction Standards (JCPDS) document numbers 0720-99 and 0056-1. The intense (111) derivative peaks are attributed to the rapid deposition of Au and Ag atoms in the (111) planes to create a branched structure [46]. Atomic force microscopy (AFM) imaging showed that the height distribution map of the A@P-M nanocomposites ranged from about 80 nm at the highest point, while the rest of the portion was below 5 nm (Fig. S1). This is caused by the large diameter of the PDA-encapsulated AuAg branched spheroidal material and the low height of the MoS_2 nanosheets adhering to its surface. FTIR results show that special peaks are observed at 804 cm^{-1} and 777 cm^{-1} for A@P-M and MoS_2, which may be due to the stretching vibration of Mo-S binding. The special peaks observed near 1342 cm^{-1} and 1633 cm^{-1} for AuAg NPs and A@P-M may originate from the stretching vibration of C=C and the bending vibration of N-H. The FTIR results showed that the AuAg@PDA-MoS_2 showed the formation of S-O bond at 1103 cm^{-1}, which was not present in the AuAg@PDA and MoS_2. It is possible that the S-O bond was formed between MoS_2 and the hydroxyl group on the surface of PDA during the reaction process, which further enhanced the bonding between the nanoparticles and molybdenum disulfide (Fig. 1D) [47].The UV spectra of A@P and A@P-M showed obvious absorption peaks at 693 nm and 700 nm, consistent with the results of previous studies (Fig. S3) [46]. The zeta potential shows that A@P-M is negatively charged and MoS_2 is positively charged, with positive and negative attraction between the two making the combination more stable (Fig. 1F). Also, in the particle size characterization of the material showed that the particle size of the majority (>55 %) of the AuAg@PDA-MoS_2 is between 100 and 400 nm (Fig. 1G). The particle size of the small percentage (<10 %) is larger than 500 nm. The wider range of particle size distributions may be related to the fragmentation and folding of ultrathin sheets of molybdenum disulfide nanosheets due to the storage and high-speed stirring during

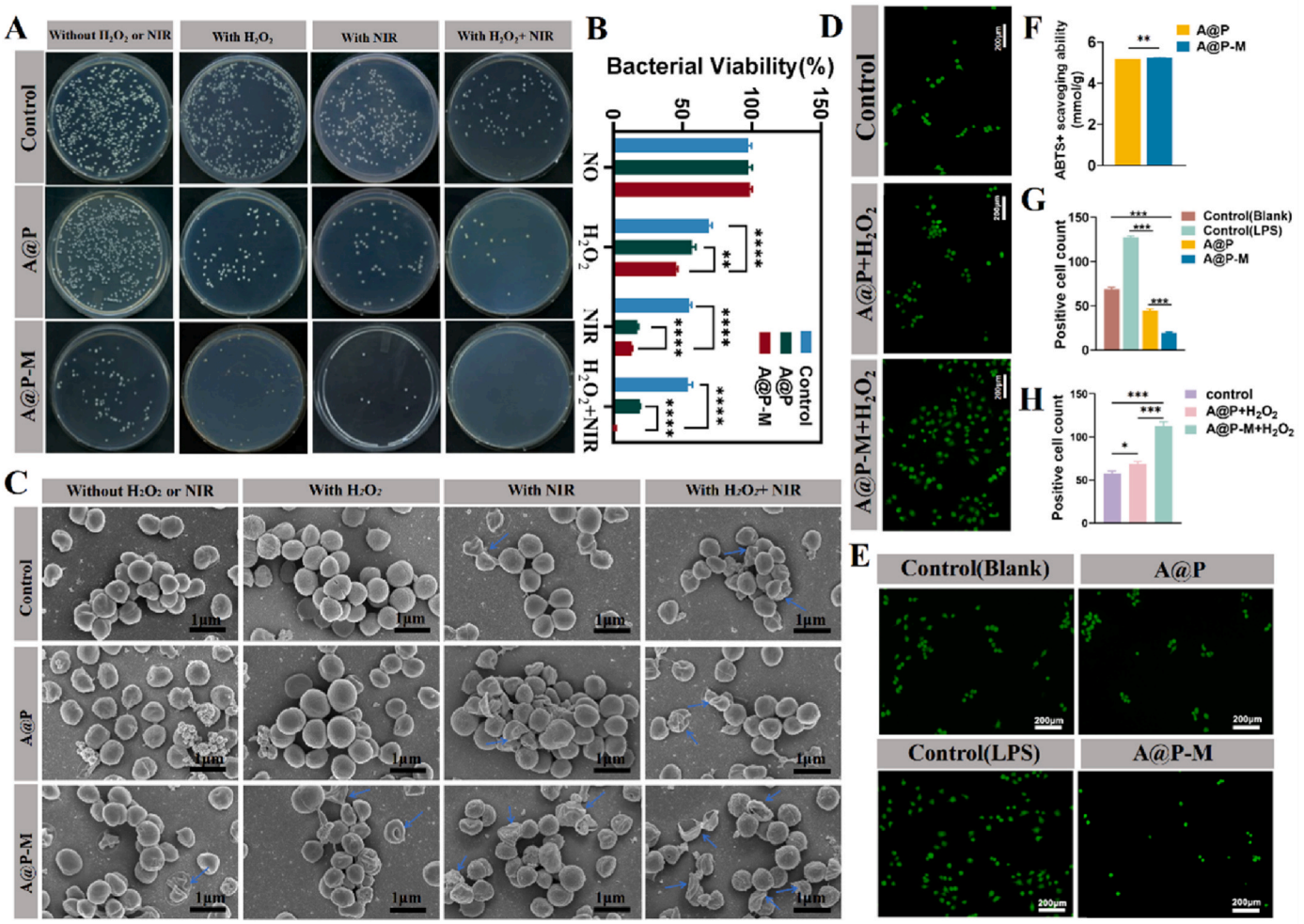

Fig. 4. (A) Images of *S. aureus* colonies after various treatment. (B) Quantification of *S. aureus* colonies after various treatment. (C) SEM images of *S. aureus*. (D) ROS scavenging activities of A@P NPs and A@P-M NPs with H_2O_2. (E) ROS scavenging activities. (F) The antioxidant activity of A@P NPs and A@P-M NPs. (G) The quantitative analysis of the ROS scavenging capacity of A@P NPs and A@P-M NPs. (H) The quantitative analysis of the ROS scavenging capacity of A@P NPs and A@P-M NPs with H_2O_2.

synthesis of A@P-M.

2.2. Photothermal performance assay

The photothermal properties of the materials were measured. The photothermal properties were examined for 20, 40, 60, 80,100 and 150 μg/ml of A@P-M (2 W/cm^2), showing a concentration-dependent photothermal effect (Fig. 2A and B). The temperature of 100 μg/ml A@P-M reached 48.2 °C after 10 min of 808 nm NIR irradiation (2 W/cm^2), which was able to kill most of bacteria while minimising damage to normal cells (Fig. 2A and B). In addition, the photothermal effect of A@P-M NPs is power dependent. The temperature of 100 μg/ml A@P-M NPs reached after 10 min of irradiation gradually increased with the increasing power (Fig. 2C). Simultaneously we compared the photothermal conversion capacity of A@P-M with water, AuAg and A@P NPs (Fig. 2D). This result showed that the A@P-M group had the best photothermal effect compared to the other groups, which was due to the addition of MoS_2 nanosheets in the A@P-M group with respect to the control group, where the 2D sheet material had a higher specific surface area. In addition, the stability of the photothermal performance of A@P-M (100 μg/ml) under three cycles of light irradiation (2 W/cm^2) was observed at 25 °C (Fig. 2E). The results showed that the photothermal performance remained stable after three irradiation cycles with 808 nm NIR.

2.3. Peroxidase-mimicking activity of A@P-M NPs

MoS_2 exhibits peroxidase-mimicking activity that converts H_2O_2 into toxic free radicals under acidic conditions. This property allows to oxidize Tetramethylbenzidine (TMB) to oxidized 3,3′,5,5′-tetramethylbenzidine (oxTMB) in the presence of H_2O_2, eventually forming a blue liquid [48]. The ability to mimic peroxidase could be determined by detecting the special peak of oxTMB at 652 nm by a UV spectral detector [49]. As the concentration of A@P-M increases, the color of the solution becomes darker blue, and the absorption peak at 652 nm becomes more obvious. This indicates that TMB is oxidized to oxTMB by the A@P-M, and the higher the concentration of the A@P-M, the more obvious the oxidation effect (Fig. 2F). By comparison, no significant color change was seen in the PBS group. In addition, when the material concentration and TMB concentration were fixed, the absorption peak at 652 nm increased significantly with the increase of H_2O_2 concentration (Fig. 2G), which indicated that the simulated peroxidase activity of the material was also dependent on the H_2O_2 concentration.

2.4. Biocompatibility and intracellular ROS tests of A@P-M NPs

The CCK8 assay showed no significant toxicity to L929 cells, which was observed in the presence of the AuAg, A@P, and A@P-M NPs at different concentrations. Still, the overall cell viability was relatively

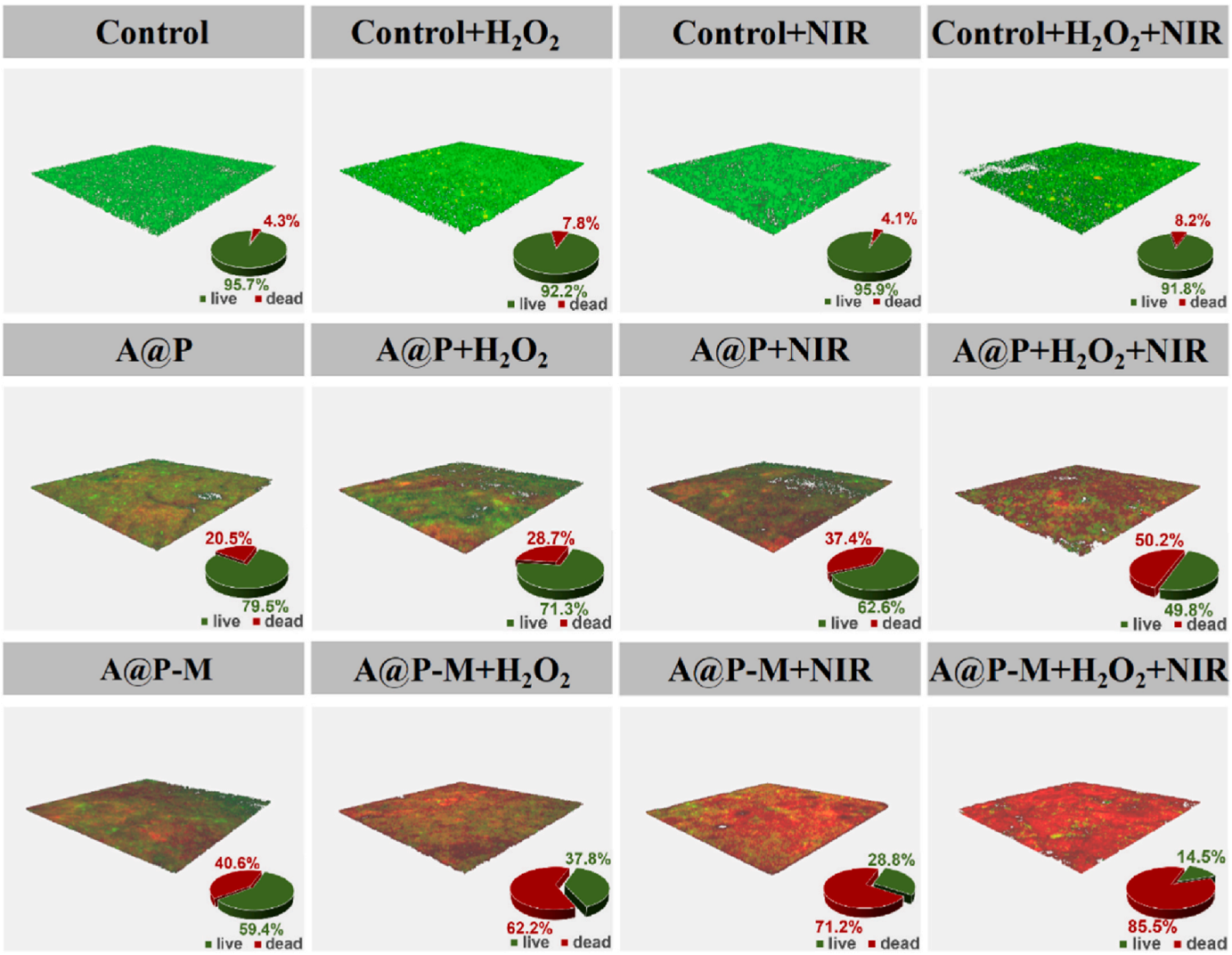

Fig. 5. 3D live/dead staining images of biofilms for *S. aureus* after different treatments. (green and or red parts in pie charts represent the proportion of live or dead bacteria.). (For interpretation of the references to color in this figure legend, the reader is referred to the Web version of this article.)

reduced when the concentration was 150 μg/mL (Fig. 3C). In addition, the cell viability was lower in the AuAg NPs group compared to the A@P and A@P-M groups. This is attributed to the certain cytotoxicity of the AuAg NPs. However, there was a significant elevation of cell viability after co-culturing with the material after wrapping the PDA shell, which is related to the excellent biocompatibility of PDA. Therefore, in order to minimize the cytotoxicity of the nanomaterials while ensuring excellent photothermal performance, 100 μg/ml of A@P-M was selected for the subsequent antibacterial and anti-inflammatory experiments. The toxicity of different concentrations of AuAg, A@P, and A@P-M NPs was tested by live-dead staining (Fig. 3A). When the concentration was 100 μg/ml, the AuAg NPs group showed the highest number of red-stained cells. In contrast, the A@P-M group showed relatively less cytotoxicity, with the least number of red-stained cells and the highest number of green-stained live cells (Fig. 3A and E). It has been proved that the biocompatibility of A@P-M NPs is better than the A@P and AuAg NPs, which is consistent with the results of CCK-8 test. There is no obvious cytotoxicity of A@P and A@P-M after NIR irradiation, which indicate that 808 nm NIR irradiation do not induce obvious toxicity to the L929 cells. Finally, based on the photothermal properties and biocompatibility of A@P-M, we chose to perform 10 min of 2.0 W/cm^2 808 NIR irradiation on 100 μg/ml of AuAg, A@P and A@P-M for subsequent experiments.

2.5. Anti-bacterial properties of A@P-M NPs

MoS_2 nanosheets can mimic peroxidase activity and serve as antioxidant catalysts to reduce the damage caused by ROS [50,51]. In this paper, DCFH-DA probe was used to monitor ROS levels. The number of positive cells detected by the probe in the A@P-M group was significantly reduced compared to the blank group as well as the LPS-stimulated group, suggesting that A@P-M NPs effectively removed the intracellular ROS levels (Fig. 4E and G). The relatively low ROS removal rate in the A@P group suggests that the antioxidant capacity of A@P-M is attributed to the MoS_2 nanosheets on the surface of the material, which is in consistent with the previous studies [36,52,53]. The antioxidant capacity of A@P-M was determined by 2,2′-Azino-bis (3-ethylbenzothiazoline-6-sulfonic acid) (ABTS) method. The results showed that the total antioxidant capacity of A@P and A@P-M in weakly acidic environment was 5.17 and 5.25 mmol/g, respectively, which confirmed the promising ROS scavenging capacity of the A@P-M group (Fig. 4F). In addition, the concentration of H_2O_2 is not sufficient for A@P-M to fully utilise its POD activity in the weak acidic environment where bacteria live. Therefore, we added additional H_2O_2 in order to achieve that A@P-M fully exerts its POD activity for producing enough •OH to kill bacteria. The ability of A@P-M to decompose H_2O_2 to produce free radicals was explored by adding glacial acetic acid

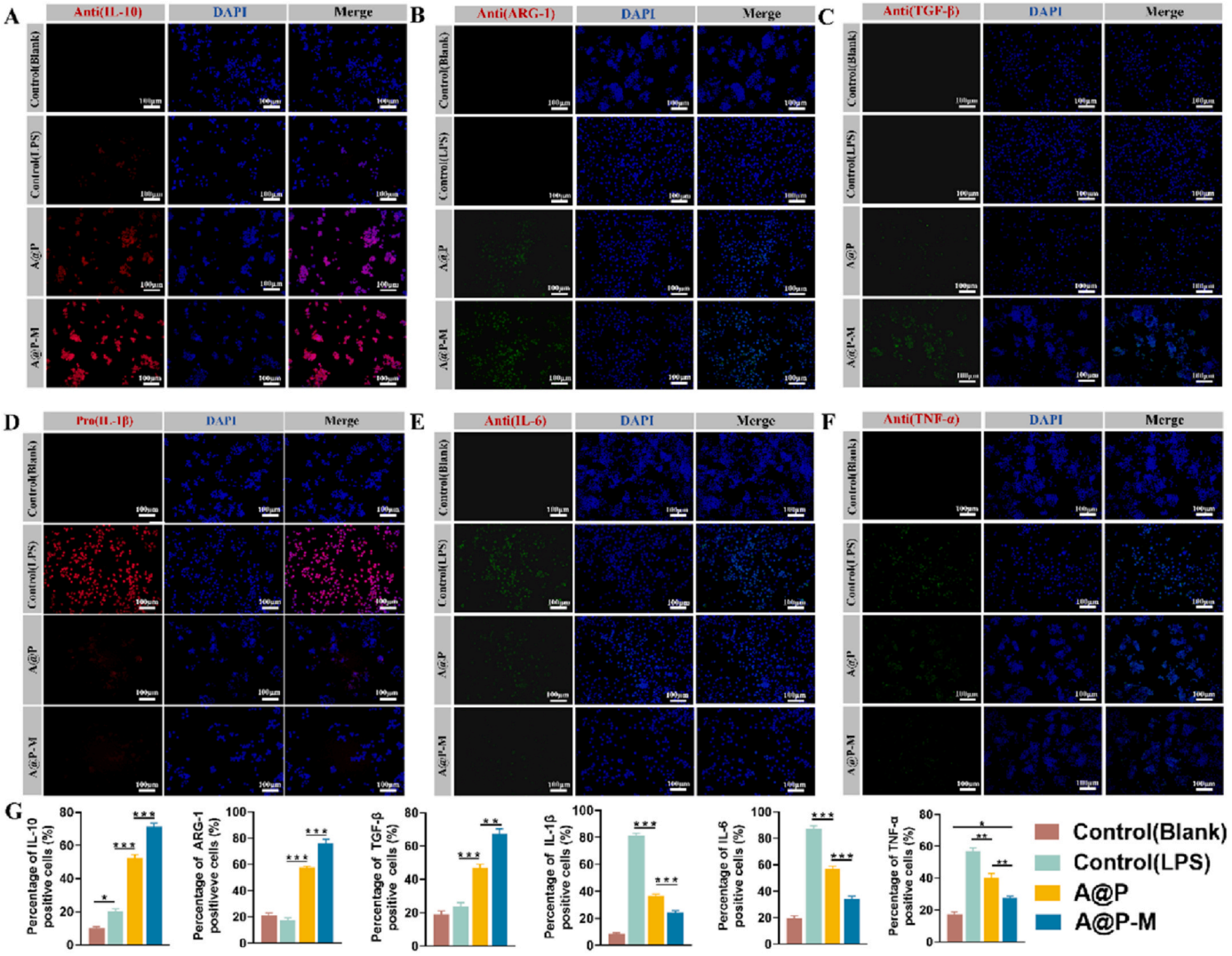

Fig. 6. IF image of (A) IL-10, (B) Arg-1, (C) TGF-β, (D) IL-1β, (E) IL-6, (F) TNF-α positive cells with different experimental treatments. (G) Quantification of corresponding positive cells with different experimental treatments.

within the medium to form a weakly acidic environment (pH = 4.0). By targeting ROS with the DCFH-DA probe we can observe that the ability of A@P-M to decompose H_2O_2 to ROS is the strongest (Fig. 4D and H).

In order to investigate the photothermal and simulated peroxidase antimicrobial properties of A@P-M, the colony-forming ability of *Staphylococcus aureus* (*S. aureus*) in the presence or absence of NIR irradiation and the presence or absence of H_2O_2 were examined. The results showed that the A@P-M NPs exhibited effective antimicrobial properties compared to the control group when there was no NIR irradiation and no H_2O_2; the antimicrobial effect of A@P-M NPs was higher in the groups of H_2O_2 or NIR irradiation (Fig. 4A and B). In addition, although the survival rates of *S. aureus* were significantly reduced in all the groups with the NIR irradiation and H_2O_2 stimulation.In the A@P-M group, the bacterial survival rate decreased to about 1 % when NIR irradiation was used simultaneously with adding H_2O_2, which shown the strongest antimicrobial effect (Fig. 4B). Thus, A@P-M composites have a desirable antimicrobial effect. Furthermore, SEM was performed to observe the changes in bacterial morphology. As shown in Fig. 4C, the morphology of *S. aureus* in the A@P-M group was disrupted compared to the control and A@P groups. However, with both H_2O_2 and NIR stimulation, the remarkable defects and collapses were observed in *S. aureus* in the A@P-M group, and even some of the *S. aureus* morphology was completely destroyed. This result verifies that A@P-M NPs can mimic peroxidase activity, which in turn interacts with H_2O_2 to produce toxic •OH, leading to antibacterial effects. It also further validates the important role played by NIR irradiation in the antimicrobial process. This is consistent with the experimental results described above. We hypothesize that the antibacterial mechanism of A@P-M composites including 1) The mimic peroxidase activity of MoS_2 that converts H_2O_2 into toxic •OH to disrupt the ROS balance within the bacteria, thus leading to bacterial lysis and death; 2) The high temperature generated by the photothermal conversion of the AuAg NPs as well as the PDA and MoS_2 nanosheets, which irreversibly damages the bacteria. 3) Physical damage of MoS_2 nanosheets towards the bacterial cell membrane; 4) the antibacterial effect of Ag.

Three-dimensional reconstruction of fluorescently labeled *S. aureus* biofilms was performed to determine changes in biofilm structure after different treatments in Fig. 5. Compared to the control group, partial red fluorescence was observed in the A@P and A@P + NIR groups, indicating that A@P and NIR irradiation had a moderately destructive effect on the bacterial biofilm. Wide area of red fluorescence was observed in A@P-M and A@P-M + NIR groups, in which the red fluorescence area of A@P-M + H_2O_2+NIR group was as high as 85.5 %, which was much higher than that of other groups. This indicated that A@P-M synergized with PTT could maximally hinder the formation of bacterial biofilm.

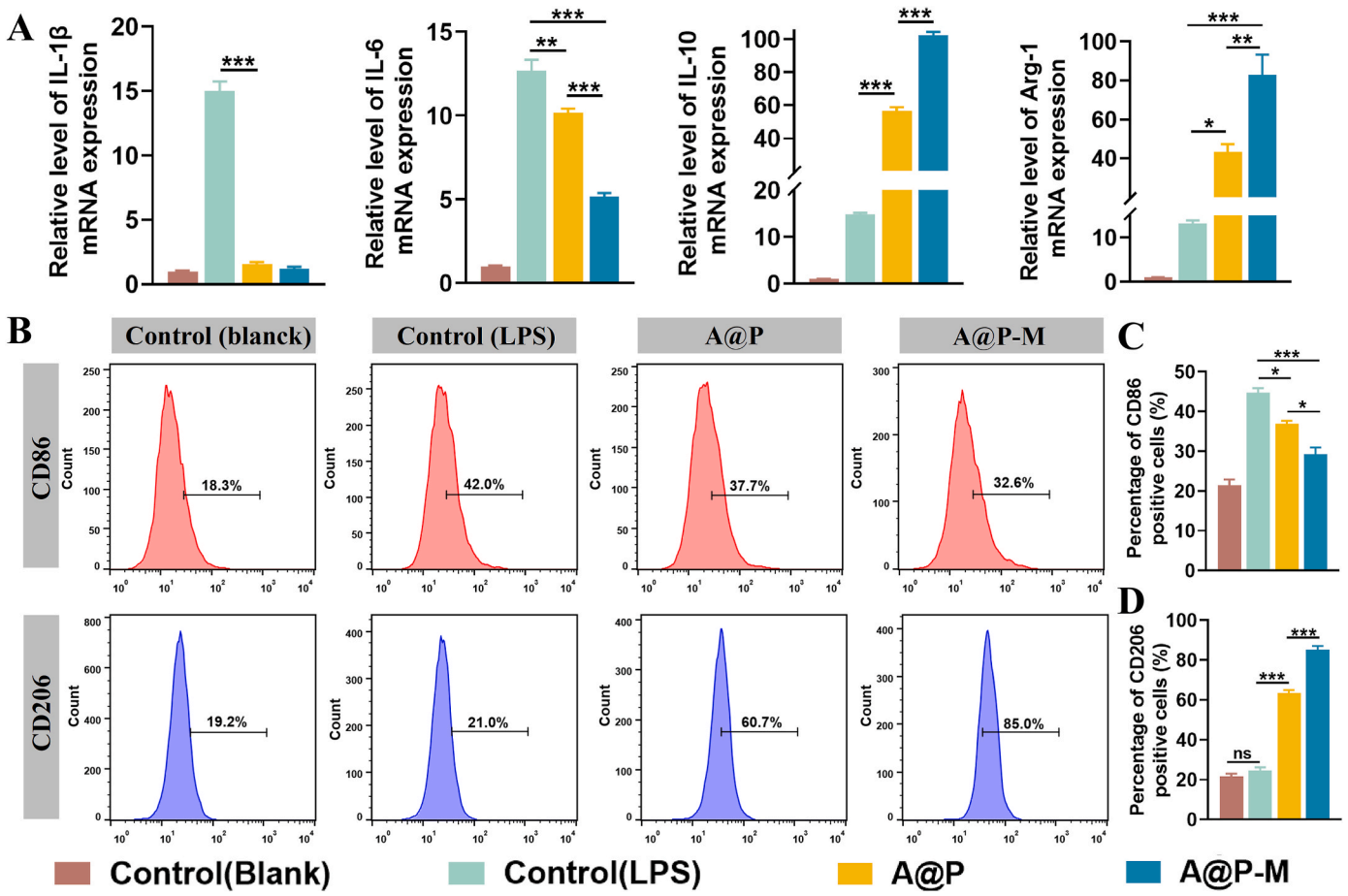

Fig. 7. (A) qPCR analysis of the gene expression of IL-1β, IL-6, IL-10, and Arg-1. (B) Detection of markers CD86 on M1 and CD206 on M2 macrophages by flow cytometry. (C) Quantifying CD86 positive cells and (D) CD206 positive cells. *p < 0.05; **p < 0.01; ***p < 0.001; ****P < 0.0001.

2.6. Anti-inflammatory properties of A@P-M NPs

Macrophages can be classified into M1 pro-inflammatory macrophages and M2 anti-inflammatory macrophages, whose phenotypic modulation can influence the development, progression, and resolution of inflammation [54]. Macrophages can transform phenotype according to different environments. M1 macrophages mainly produce massive pro-inflammatory cytokines to accelerate the development of inflammation, such as IL-1 β, TNF-α, and IL-6. In contrast, M2 macrophages primarily secrete anti-inflammatory factors, such as IL-10, TGF-β, and Arg-1, which inhibit inflammation and promote tissue remodeling and repair [55–58]. In order to investigate the regulatory effect of A@P-M on inflammation, real-time quantitative polymerase chain reaction (qPCR), flow cytometry, and Immunofluorescence (IF) staining of pro-inflammatory cytokine IL-1β, IL-6, TNF-α and anti-inflammatory cytokine IL-10, TGF-β, and Arg-1 was performed. The results showed that the expression of pro-inflammatory factor IL-1β, IL-6 and TNF-α was significant higher under LPS stimulation, while the expression of pro-inflammatory factors in the A@P-M group was not evident, especially IL-1β was little expressed in the A@P-M group (Fig. 6D–F). As for the anti-inflammatory factor IL-10, TGF-β, and Arg-1, the expression was significantly higher in the A@P group, which was most pronounced in the A@P-M group (Fig. 6A–C). Relevant semiquantities analysis have been shown in Fig. 6G, which is attributed to the fact that Mo element, involved in redox reactions, exists in three oxidation states (+4, +5, +6). Meanwhile, Mo, as a trace element, is the catalytic center of many enzymes, catalyzing redox and oxygen transfer reactions [59]. Thus, the A@P-M group promotes the expression of anti-inflammatory factors, thereby exerting an anti-inflammatory effect.

The results of qPCR are shown in Fig. 7A. After LPS stimulation, the levels of pro-inflammatory cytokines IL-1β and IL-6 secreted by M1 macrophages were dramatically increased, whereas the expression of these pro-inflammatory cytokines was greatly inhibited by A@P-M NPs. In contrast, A@P-M NPs significantly increased the expression of anti-inflammatory factors IL-10 and Arg-1 compared to the Control (LPS) and A@P NPs groups. The ratios of surface markers CD86 on M1 type macrophages and CD206 on M2 type macrophages were examined by flow cytometry (Fig. 7B), respectively. The results showed that A@P-M suppressed the expression of CD86 that up-regulated by LPS (32.6 %) compared with the Control (LPS) group (42.0 %) (Fig. 7C). Meanwhile, A@P-M significantly promoted the expression of CD206 in macrophages (85.0 %) compared with the A@P group (60.7 %) and the Control (LPS) group (21.0 %) (Fig. 7D). These results suggest that A@P-M NPs can effectively regulate the polarisation of M1 and M2 macrophages, which in turn suppresses to the development of inflammation through immunomodulation.

2.7. Metabolomics analysis of A@P-M NPs

Metabolomics analyses revealed a total of 116 differential metabolites in *S. aureus* between the control and A@P-M groups, which contained 73 down-regulated metabolites and 43 up-regulated metabolites (Fig. 8A and C). KEGG pathway analyses revealed significant down-regulation of the citric acid cycle (TCA cycle), ABC transporter proteins, and biosynthesis (Fig. 8B and D). In addition, molecules related to nucleoside metabolism (purines and pyrimidines), as well as amino acid metabolism (alanine, threonine, aspartic acid, glycine, serine, glutamate, and arginine) were significantly down-regulated after A@P-M

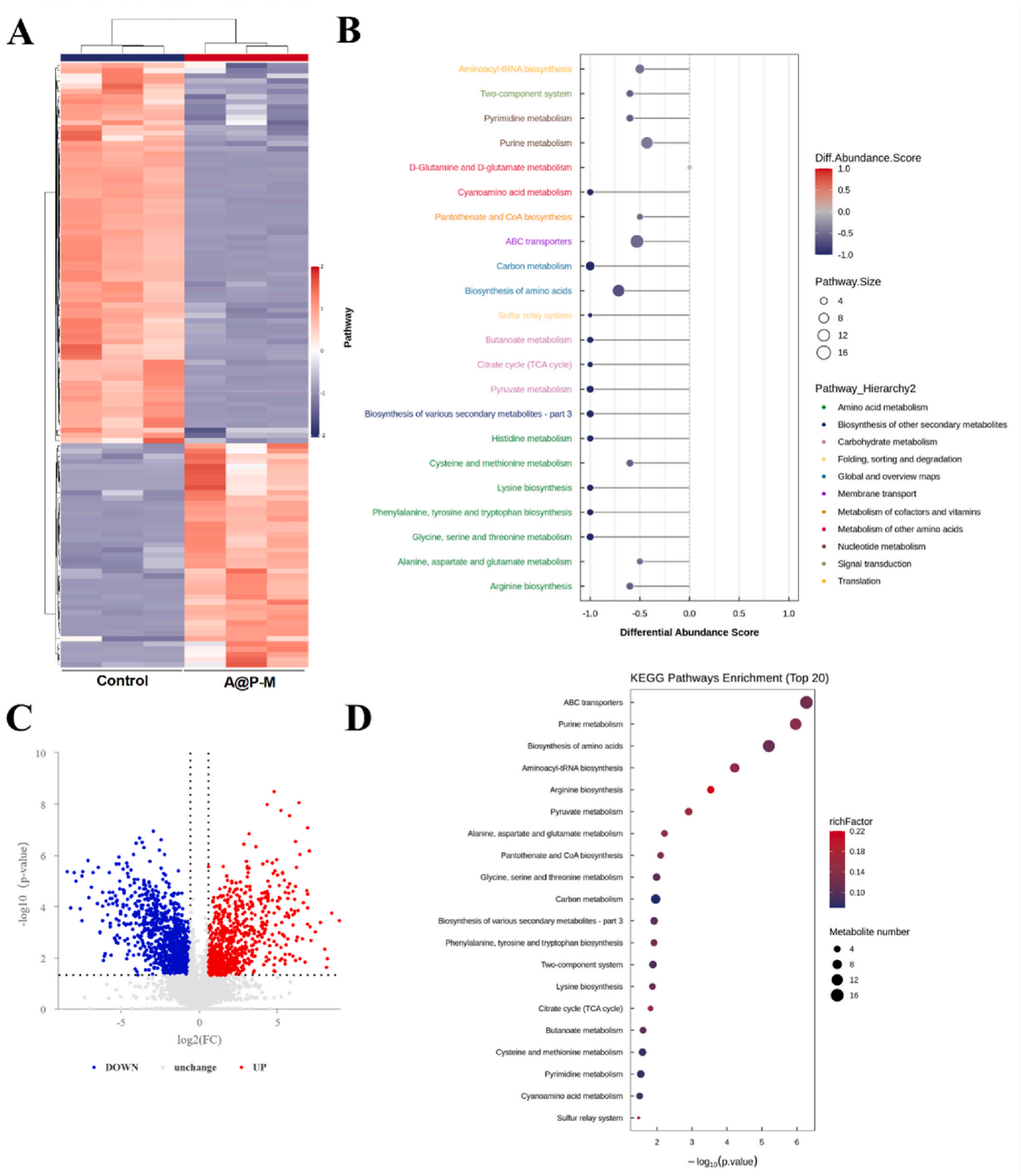

Fig. 8. (A) Heat map of metabolomics. (B) Down-regulated terms analyzed by the enriched KEGG pathways. (C) Volcano plot of metabolomics. (D) KEGG enrichment pathway map of metabolomics.

treatment (Fig. 8B and D). Meanwhile nucleotides, purines and pyrimidines are essential for DNA synthesis. Therefore, we hypothesize that A@P-M NPs inhibits *S. aureus* growth through inhibition of DNA synthesis.

2.8. Evaluation for promoting wound healing in vivo

To further validate the ability of A@P-M to promote wound healing, an infected whole-layer wound healing model was established. To

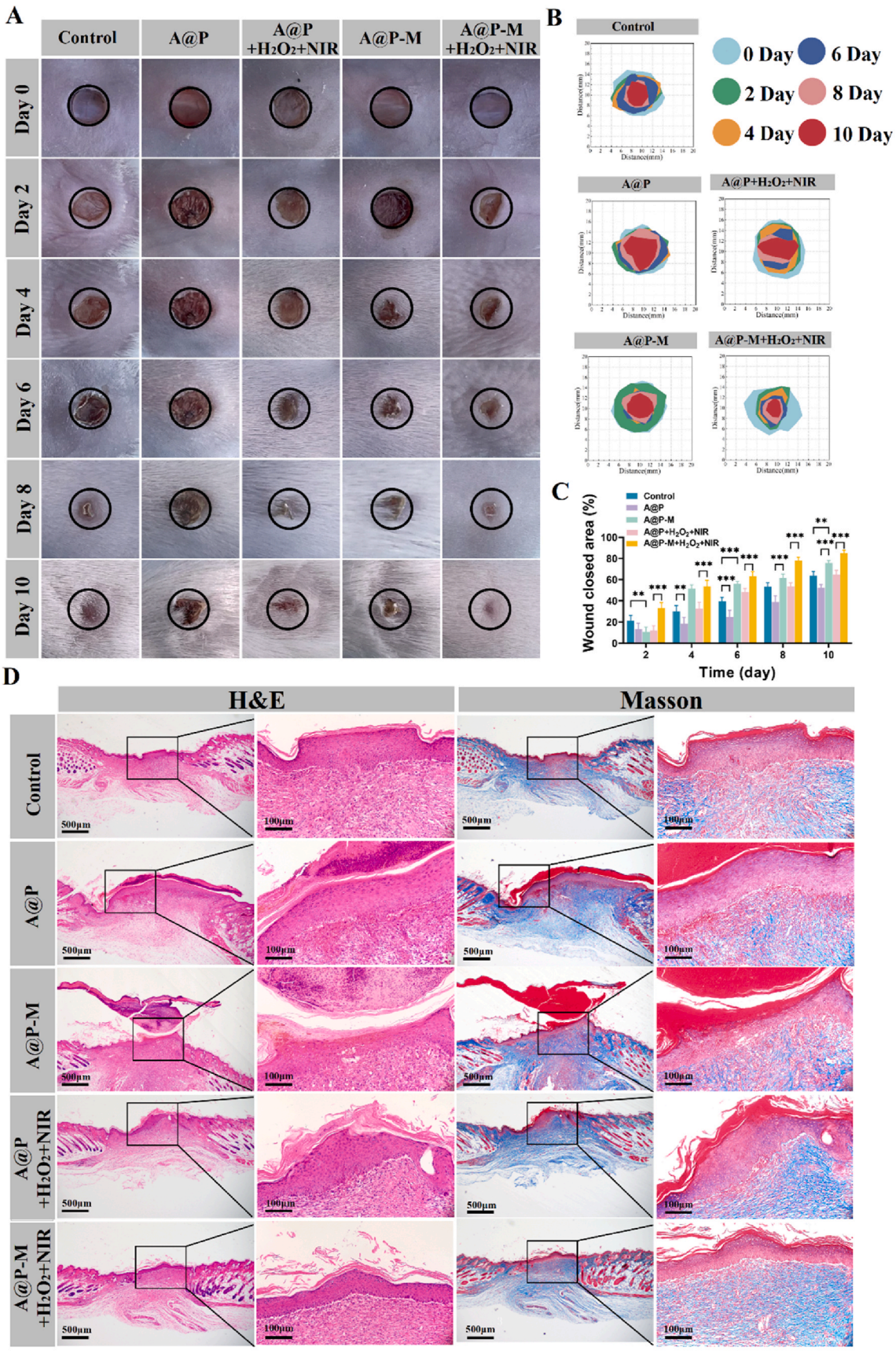

Fig. 9. (A) Representative images of the wound healing process of mice in different groups. (B) The corresponding traces of control, A@P, A@P-M, A@P + H_2O_2+NIR and A@P-M + H_2O_2+NIR groups at 0, 2, 4, 6, 8 and 10d. (C) Wound closure rate of control, A@P, A@P-M, A@P + H_2O_2+NIR and A@P-M + H_2O_2+NIR groups at 0, 2, 4, 6, 8 and 10d. (D) H&E and Masson staining images of the epidermal histological sections in different groups.

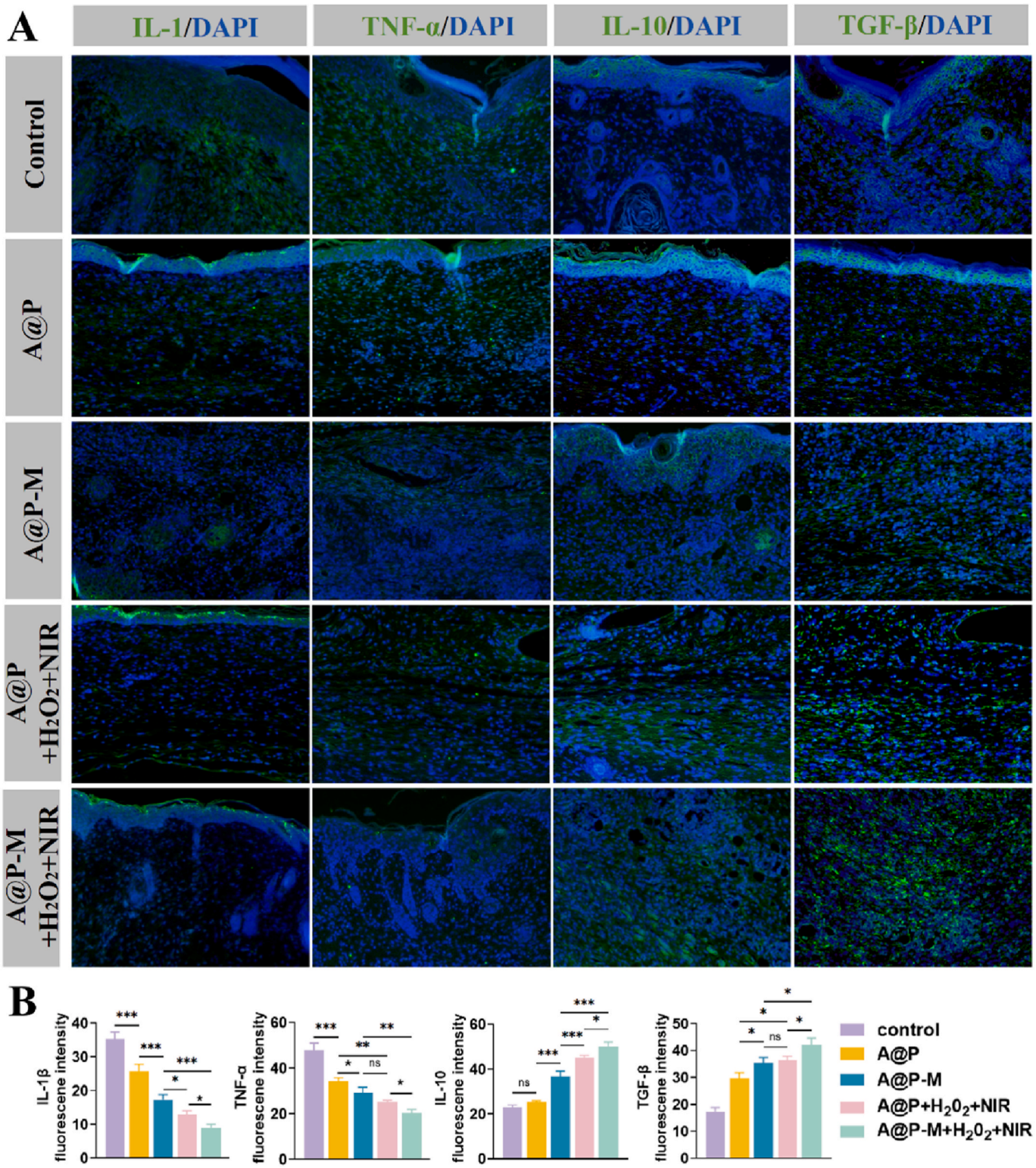

Fig. 10. (A) Immunofluorescence images of IL-1, TNF-α, IL-10 and TGF-β expressed in wounds. (B) Quantitative analysis for the fluorescence intensity.

demonstrate the antimicrobial healing-promoting effect of photothermal action synergistically mimicking peroxidase activity, the control group, A@P group, A@P + H_2O_2+NIR group, A@P-M group, and A@P-M + H_2O_2+NIR group were set up in the in *vivo* experiments. After two days, both the A@P + H_2O_2+NIR group and the A@P-M + H_2O_2+NIR group significantly improved wound healing compared with the other two groups. In addition, the A@P-M group and the A@P-M + H_2O_2+NIR group showed the best wound healing ability throughout the consecutive wound healing experiments, with remaining unhealed wound areas of about 24.8 % and about 15 %, respectively (Fig. 9A and C). In contrast, the wound healing in the A@P group and the A@P + H_2O_2+NIR group were slower, with the proportion of remaining unhealed wounds around 47 % and 35 %, respectively. Secondly, it can be found that the A@P-M + H_2O_2+NIR group has the smallest area of

unhealed wounds and the best healing situation by observing the wound healing superposition diagram (Fig. 9B), which is consistent with the conclusions of in *vitro* experiments.

We further explored the histologic staining results of different antimicrobial materials. Hematoxylin and eosin (H&E) staining is shown in (Fig. 9D). The A@P-M + H_2O_2+NIR group showed the best wound healing and integrity of the epidermis, where continuous epithelium was observed, showing better tissue regeneration. This was attributed to the combination of antimicrobial and anti-inflammatory properties of the composite nanomaterials due to the mimetic enzyme activity of MoS_2 and PTT of NIR irradiation, which promoted the regeneration of dermal tissues. The biotoxicity of A@P-M NPs was further assessed by H&E staining of the heart, liver, spleen, lungs and kidneys in a 10-day animal model (Fig. S4). Sections indicated no histologic and morphological differences between the A@P-M group and the control group. Therefore, the 100 μg/mL A@P-M NPs has a favored biosafety in *vivo*. Masson staining was also performed to evaluate further the wound repair process (Fig. 9D), which could observe more collagen deposition in the A@P-M + H_2O_2+NIR group, confirming a better therapeutic effect. After 10 days of treatment in different groups, compared with the results of the A@P-M group and A@P-M + H_2O_2+NIR group, the wound healing was slow in A@P and A@P + H_2O_2+NIR groups which the remaining unhealed wounds accounted for 47 % and 35 % of the original wound area, respectively (Fig. 9A and C). However, the proportion was about 24.8 % and about 15 %, respectively in the A@P-M group and A@P-M + H_2O_2+NIR group. by observing the wound healing superimposed graph (Fig. 9B) it can also be found that the A@P-M + H_2O_2+NIR group had the smallest wound area and healed well, which were similar to the conclusions of the in *vitro* experiments. A@P-M + H_2O_2+NIR could promote wound healing.

IF staining of subcutaneous tissues was performed to observe the immunomodulatory capacity mediated by A@P-M (Fig. 10A). Significantly lower expression signals of pro-inflammatory cytokines (IL-1βand TNF-α) and significant fluorescence signals of related anti-inflammatory cytokines (IL-10 and TGF-β) were observed in subcutaneous tissues after the treatment of A@P-M for 14 days (Fig. 10B), which confirmed the immunomodulatory potential of A@P-M.

3. Conclusion

In conclusion, the A@P-M NPs were prepared, which were loaded with MoS_2 after PDA wrapped with AuAg bimetal. In terms of antimicrobial activity, A@P-M mimics peroxidase activity through the interconversion of Mo ions in different valence states, to be specific, Mo^{4+} has peroxidase-mimicking activity, which reacts with endogenous H_2O_2 to produce •OH and Mo^{6+}. In turn, Mo^{6+} can oxidize glutathione, accelerating the consumption of glutathione by reverting itself to Mo^{4+}. This cycling of Mo^{4+} and Mo^{6+} ultimately induces the production of large amounts of •OH, which can constitute an excellent antimicrobial platform. Meanwhile, A@P-M NPs killed *S. aureus* by synergizing PTT and PDT. In the anti-inflammatory aspect, it can play an anti-inflammatory role by regulating the cytokines secreted by macrophages and steering macrophages polarisation towards the M2 phenotype. The dual therapeutic action of A@P-M NPs has potential applications in accelerating the healing process of biofilm-infected wounds. However clinical evaluations are necessary to validate and optimise the translational prospects of such an innovative nanoparticle-based therapeutic approach.

CRediT authorship contribution statement

Zhen Yang: Investigation, Formal analysis, Conceptualization. **Jiaqian You:** Validation, Supervision, Resources, Project administration, Investigation. **Shaobo Zhai:** Conceptualization. **Jing Zhou:** Data curation, Conceptualization. **Sezhen Quni:** Software. **Manxuan Liu:** Conceptualization. **Lu Zhang:** Conceptualization. **Rui Ma:** Conceptualization. **Qiuyue Qin:** Conceptualization. **Huimin Huangfu:** Conceptualization. **Yidi Zhang:** Conceptualization. **Yanmin Zhou:** Funding acquisition, Formal analysis, Conceptualization.

Declaration of competing interest

The authors declare that they have no known competing financial interests or personal relationships that could have appeared to influence the work reported in this paper.

Acknowledgements

Z.Y. and J.Y. contributed equally to this work. The authors acknowledge the support from the National Natural Science Foundation of China (Grant No. 82001092; Grant No. 82071152). All animal procedures were conducted under the Guidelines for Care and Use of Laboratory Animals of Jilin University and approved by the College of Basic Medicine of Jilin University (Permit Number:2023494)

Appendix A. Supplementary data

Supplementary data to this article can be found online at https://doi.org/10.1016/j.mtbio.2025.101481.

Data availability

Data will be made available on request.

References

[1] J.G. Powers, C. Higham, K. Broussard, T.J. Phillips, Wound healing and treating wounds: chronic wound care and management, J. Am. Acad. Dermatol. 74 (4) (2016) 607–625, quiz 625-625.
[2] J. He, Y. Liang, M. Shi, B. Guo, Anti-oxidant electroactive and antibacterial nanofibrous wound dressings based on poly(ε-caprolactone)/quaternized chitosan-graft-polyaniline for full-thickness skin wound healing, Chem. Eng. J. 385 (2020) 123464.
[3] K.E. Jones, N.G. Patel, M.A. Levy, A. Storeygard, D. Balk, J.L. Gittleman, P. Daszak, Global trends in emerging infectious diseases, Nature 451 (7181) (2008) 990–993.
[4] H. Zhao, J. Huang, Y. Li, X. Lv, H. Zhou, H. Wang, Y. Xu, C. Wang, J. Wang, Z. Liu, ROS-scavenging hydrogel to promote healing of bacteria infected diabetic wounds, Biomaterials 258 (2020) 120286.
[5] G. Xu, Y. Lu, C. Cheng, X. Li, J. Xu, Z. Liu, J. Liu, G. Liu, Z. Shi, Z. Chen, F. Zhang, Y. Jia, D. Xu, W. Yuan, Z. Cui, S.S. Low, Q. Liu, Battery-free and wireless smart wound dressing for wound infection monitoring and electrically controlled on-demand, Drug Deliv. 31 (26) (2021) 2100852.
[6] E.D. Hermsen, E.L. MacGeorge, M.L. Andresen, L.M. Myers, C.J. Lillis, B.M. Rosof, Decreasing the peril of antimicrobial resistance through enhanced health literacy in outpatient settings: an underrecognized approach to advance antimicrobial stewardship, Adv. Ther. 37 (2) (2020) 918–932.
[7] Y. Zhang, P. Huang, D. Wang, J. Chen, W. Liu, P. Hu, M. Huang, X. Chen, Z. Chen, Near-infrared-triggered antibacterial and antifungal photodynamic therapy based on lanthanide-doped upconversion nanoparticles, Nanoscale 10 (33) (2018) 15485–15495.
[8] J. Sun, L. Song, Y. Fan, L. Tian, S. Luan, S. Niu, L. Ren, W. Ming, J. Zhao, Synergistic photodynamic and photothermal antibacterial nanocomposite membrane triggered by single NIR light source, ACS Appl. Mater. Interfaces 11 (30) (2019) 26581–26589.
[9] H. Wang, Z. Song, S. Li, Y. Wu, H. Han, One stone with two birds: functional gold nanostar for targeted combination therapy of drug-resistant Staphylococcus aureus infection, ACS Appl. Mater. Interfaces 11 (36) (2019) 32659–32669.
[10] Y. Liang, Y. Liang, H. Zhang, B. Guo, Antibacterial biomaterials for skin wound dressing, Asian J. Pharm. Sci. 17 (3) (2022) 353–384.
[11] Y. Yu, P. Li, C. Zhu, N. Ning, S. Zhang, G.J. Vancso, Multifunctional and recyclable photothermally responsive cryogels as efficient platforms for wound healing 29 (35) (2019) 1904402.
[12] W.C. Martins Antunes de Melo, R. Celiešiūtė-Germanienė, P. Šimonis, A. Stirkė, Antimicrobial photodynamic therapy (aPDT) for biofilm treatments. Possible synergy between aPDT and pulsed electric fields, Virulence 12 (1) (2021) 2247–2272.
[13] Y. Chen, Q. Ji, G. Zhang, H. Liu, J. Qu, Synergetic lipid extraction with oxidative damage amplifies cell-membrane-destructive stresses and enables rapid sterilization, Angew. Chem. 60 (14) (2021) 7744–7751.
[14] X. Lin, Y. Fang, Z. Hao, H. Wu, M. Zhao, S. Wang, Y. Liu, Bacteria-Triggered multifunctional hydrogel for localized chemodynamic and low-temperature photothermal sterilization, Small 17 (51) (2021) e2103303.
[15] Y. Zhao, X. Dai, X. Wei, Y. Yu, X. Chen, X. Zhang, C. Li, Near-infrared light-activated thermosensitive liposomes as efficient agents for photothermal and

antibiotic synergistic therapy of bacterial biofilm, ACS Appl. Mater. Interfaces 10 (17) (2018) 14426–14437.
[16] F. Wang, Q. Wu, G. Jia, L. Kong, R. Zuo, K. Feng, M. Hou, Y. Chai, J. Xu, C. Zhang, Q. Kang, Black phosphorus/MnO2 nanocomposite disrupting bacterial thermotolerance for efficient mild-temperature photothermal therapy 10 (30) (2023) 2303911.
[17] G. Ma, Z. Liu, C. Zhu, H. Chen, R.T.K. Kwok, P. Zhang, B.Z. Tang, L. Cai, P. Gong, H2O2-Responsive NIR-II AIE nanobomb for carbon monoxide boosting low-temperature photothermal therapy 61 (36) (2022) e202207213.
[18] W. Liu, J. Di, Y. Ma, S. Wang, M. Meng, Y. Yin, R. Xi, X. Zhao, Mitochondria-mediated HSP inhibition strategy for enhanced low-temperature photothermal therapy, ACS Appl. Mater. Interfaces 15 (22) (2023) 26252–26262.
[19] X. Wang, M. Shan, S. Zhang, X. Chen, W. Liu, J. Chen, X. Liu, Stimuli-responsive antibacterial materials: molecular structures, design principles, and biomedical applications, Adv. Sci. 9 (13) (2022) e2104843.
[20] L. Guo, Y. Tian, L. Zhou, S. Kang, C. Zhang, W. Liu, H. Diao, L. Feng, Tailored phototherapy agent by infection site in situ activated against methicillin-resistant S. aureus, Adv Healthc Mater (2024) e2400593.
[21] L. Feng, C. Li, L. Liu, Z. Wang, Z. Chen, J. Yu, W. Ji, G. Jiang, P. Zhang, J. Wang, B. Z. Tang, Acceptor planarization and donor rotation: a facile strategy for realizing synergistic cancer phototherapy via type I PDT and PTT, ACS Nano 16 (3) (2022) 4162–4174.
[22] Y. Liu, Y. Tian, Q. Han, J. Yin, J. Zhang, Y. Yu, W. Yang, Y. Deng, Synergism of 2D/1D MXene/cobalt nanowire heterojunctions for boosted photo-activated antibacterial application, Chem. Eng. J. 410 (2021) 128209.
[23] Z. Gan, Z. Xiao, Z. Zhang, Y. Li, C. Liu, X. Chen, Y. Liu, D. Wu, C. Liu, X. Shuai, Y. Cao, Stiffness-tuned and ROS-sensitive hydrogel incorporating complement C5a receptor antagonist modulates antibacterial activity of macrophages for periodontitis treatment, Bioact. Mater. 25 (2023) 347–359.
[24] G. Applerot, A. Lipovsky, R. Dror, N. Perkas, Y. Nitzan, R. Lubart, A. Gedanken, Enhanced antibacterial activity of nanocrystalline ZnO due to increased ROS-mediated, Cell Injury 19 (6) (2009) 842–852.
[25] Z. Wang, R. Jia, Y. Chen, X. Xie, S. Wang, J. Huang, M. Zhou, K. Cai, J. Zhang, Supramolecular semiquinone radicals confined with DNAzymes for dissipative ROS generation and therapy, Nano Today 43 (2022) 101402.
[26] C. Geng, S. He, S. Yu, H.M. Johnson, H. Shi, Y. Chen, Y.K. Chan, W. He, M. Qin, X. Li, Y. Deng, Achieving clearance of drug-resistant bacterial infection and rapid cutaneous wound regeneration using an ROS-balancing-engineered heterojunction, Advanced materials (Deerfield Beach, Fla.) 36 (16) (2024) e2310599.
[27] Y. Kang, Z. Mao, Y. Wang, C. Pan, M. Ou, H. Zhang, W. Zeng, X. Ji, Design of a two-dimensional interplanar heterojunction for catalytic cancer therapy, Nat. Commun. 13 (1) (2022) 2425.
[28] D. Yim, D.E. Lee, Y. So, C. Choi, W. Son, K. Jang, C.S. Yang, J.H. Kim, Sustainable nanosheet antioxidants for sepsis therapy via scavenging intracellular reactive oxygen and nitrogen species, ACS Nano 14 (8) (2020) 10324–10336.
[29] L. Wang, F. Gao, A. Wang, X. Chen, H. Li, X. Zhang, H. Zheng, R. Ji, B. Li, X. Yu, J. Liu, Z. Gu, F. Chen, C. Chen, Defect-rich adhesive molybdenum disulfide/rGO vertical heterostructures with enhanced nanozyme activity for smart bacterial killing application, Advanced materials (Deerfield Beach, Fla.) 32 (48) (2020) e2005423.
[30] M. Xu, Y. Hu, Y. Xiao, Y. Zhang, K. Sun, T. Wu, N. Lv, W. Wang, W. Ding, F. Li, B. Qiu, J. Li, Near-infrared-controlled nanoplatform exploiting photothermal promotion of peroxidase-like and OXD-like activities for potent antibacterial and anti-biofilm therapies, ACS Appl. Mater. Interfaces 12 (45) (2020) 50260–50274.
[31] J. Wang, Y. Hu, Q. Zhou, L. Hu, W. Fu, Y. Wang, Peroxidase-like activity of metal-organic framework [Cu(PDA)(DMF)] and its application for colorimetric detection of dopamine, ACS Appl. Mater. Interfaces 11 (47) (2019) 44466–44473.
[32] Z. Yang, X. Fu, D. Ma, Y. Wang, L. Peng, J. Shi, J. Sun, X. Gan, Y. Deng, W. Yang, Growth factor-decorated Ti3C2 MXene/MoS2 2D bio-heterojunctions with quad-channel photonic disinfection for effective regeneration of bacteria-invaded cutaneous tissue 17 (50) (2021) 2103993.
[33] Y. Li, R. Fu, Z. Duan, C. Zhu, D. Fan, Adaptive hydrogels based on nanozyme with dual-enhanced triple enzyme-like activities for wound disinfection and mimicking antioxidant defense, System 11 (2) (2022) 2101849.
[34] Z.-Y. Liao, Y.-M. Xia, J.-M. Zuo, T. Wang, D.-T. Hu, M.-Z. Li, N.-N. Shao, D. Chen, K.-X. Song, X. Yu, X.-Y. Zhang, W.-W. Gao, Metal–Organic framework modified MoS2 nanozyme for synergetic combating drug-resistant bacterial infections via photothermal effect and photodynamic modulated peroxidase-mimic activity 11 (1) (2022) 2101698.
[35] J. Li, J. Li, Y. Chen, P. Tai, P. Fu, Z. Chen, P.-S. Yap, Z. Nie, K. Lu, B. He, Molybdenum disulfide-supported cuprous oxide nanocomposite for near-infrared-I light-responsive synergistic antibacterial therapy, ACS Nano 18 (25) (2024) 16184–16198.
[36] T. Chen, H. Zou, X. Wu, C. Liu, B. Situ, L. Zheng, G. Yang, Nanozymatic antioxidant system based on MoS(2) nanosheets, ACS Appl. Mater. Interfaces 10 (15) (2018) 12453–12462.
[37] X. Li, J. Shan, W. Zhang, S. Su, L. Yuwen, L. Wang, Recent advances in synthesis and biomedical applications of two-dimensional transition metal dichalcogenide nanosheets 13 (5) (2017) 1602660.
[38] B. Xu, D. Yu, C. Xu, Y. Gao, H. Sun, L. Liu, Y. Yang, D. Qi, J. Wu, Study on synergistic mechanism of molybdenum disulfide/sodium carboxymethyl cellulose composite nanofiber mats for photothermal/photodynamic antibacterial treatment, Int. J. Biol. Macromol. 266 (2024) 130838.
[39] B. Luo, X. Li, P. Liu, M. Cui, G. Zhou, J. Long, X. Wang, Self-assembled NIR-responsive MoS2@quaternized chitosan/nanocellulose composite paper for recyclable antibacteria, J. Hazard Mater. 434 (2022) 128896.
[40] Z. Wang, Y. Fang, X. Zhou, Z. Li, H. Zhu, F. Du, X. Yuan, Q. Yao, J. Xie, Embedding ultrasmall Ag nanoclusters in Luria-Bertani extract via light irradiation for enhanced antibacterial activity, Nano Res. 13 (1) (2020) 203–208.
[41] A. Singh, K. Rani, V. Tandon, A.K. Sahoo, S.K. Samanta, Ag NCs as a potent antibiofilm agent against pathogenic Pseudomonas aeruginosa and Acinetobacter baumannii and drug-resistant Bacillus subtilis by affecting chemotaxis and flagellar assembly pathway genes, Biomater. Sci. 10 (23) (2022) 6778–6790.
[42] Y. Wang, M.J. Malkmes, C. Jiang, P. Wang, L. Zhu, H. Zhang, Y. Zhang, H. Huang, L. Jiang, Antibacterial mechanism and transcriptome analysis of ultra-small gold nanoclusters as an alternative of harmful antibiotics against Gram-negative bacteria, J. Hazard Mater. 416 (2021) 126236.
[43] L. Wang, Q. Hou, W. Zheng, X. Jiang, Fluorescent and antibacterial aminobenzeneboronic acid (ABA)-Modified gold nanoclusters for self-monitoring residual dosage and smart wound care, ACS Nano 15 (11) (2021) 17885–17894.
[44] B. Yang, D. Bin, K. Zhang, Y. Du, T. Majima, A seed-mediated method to design N-doped graphene supported gold-silver nanothorns sensor for rutin detection, J. Colloid Interface Sci. 512 (2018) 446–454.
[45] A.D. Marinov, L. Bravo Priegue, A.R. Shah, T.S. Miller, C.A. Howard, G. Hinds, P. R. Shearing, P.L. Cullen, D.J.L. Brett, Ex situ characterization of 1T/2H MoS2 and their carbon composites for energy applications, a review, ACS Nano 17 (6) (2023) 5163–5186.
[46] J. Li, W. Wang, L. Zhao, L. Rong, S. Lan, H. Sun, H. Zhang, B. Yang, Hydroquinone-assisted synthesis of branched au-ag nanoparticles with polydopamine coating as highly efficient photothermal agents, ACS Appl. Mater. Interfaces 7 (21) (2015) 11613–11623.
[47] L. Yuwen, Y. Sun, G. Tan, W. Xiu, Y. Zhang, L. Weng, Z. Teng, L. Wang, MoS(2) @polydopamine-Ag nanosheets with enhanced antibacterial activity for effective treatment of Staphylococcus aureus biofilms and wound infection, Nanoscale 10 (35) (2018) 16711–16720.
[48] K. Wang, K. Chen, T.J. Prior, X. Feng, C. Redshaw, Pd-immobilized schiff base double-layer macrocycle: synthesis, structures, peroxidase mimic activity, and antibacterial performance, ACS Appl. Mater. Interfaces 14 (1) (2022) 1423–1433.
[49] Z. Wang, J. Zhu, L. Chen, K. Deng, H. Huang, Multifunctional gold–silver–carbon quantum dots nano-hybrid composite: advancing antibacterial wound healing and cell proliferation, ACS Appl. Mater. Interfaces 15 (34) (2023) 40241–40254.
[50] W. Dong, G. Chen, X. Hu, X. Zhang, W. Shi, Z. Fu, Molybdenum disulfides nanoflowers anchoring iron-based metal organic framework: a synergetic catalyst with superior peroxidase-mimicking activity for biosensing, Sensor. Actuator. B Chem. 305 (2020) 127530.
[51] L. Wan, L. Wu, S. Su, D. Zhu, J. Chao, L. Wang, High peroxidase-mimicking activity of gold@platinum bimetallic nanoparticle-supported molybdenum disulfide nanohybrids for the selective colorimetric analysis of cysteine, Chemical communications (Cambridge, England) 56 (82) (2020) 12351–12354.
[52] Y. Li, R. Fu, Z. Duan, C. Zhu, D. Fan, Adaptive hydrogels based on nanozyme with dual-enhanced triple enzyme-like activities for wound disinfection and mimicking antioxidant defense system, Adv Healthc Mater 11 (2) (2022) e2101849.
[53] Z.Y. Liao, Y.M. Xia, J.M. Zuo, T. Wang, D.T. Hu, M.Z. Li, N.N. Shao, D. Chen, K. X. Song, X. Yu, X.Y. Zhang, W.W. Gao, Metal-Organic framework modified MoS(2) nanozyme for synergetic combating drug-resistant bacterial infections via photothermal effect and photodynamic modulated peroxidase-mimic activity, Adv Healthc Mater 11 (1) (2022) e2101698.
[54] P.J. Murray, Macrophage polarization, Annu. Rev. Physiol. 79 (2017) 541–566.
[55] A. Viola, F. Munari, R. Sánchez-Rodríguez, T. Scolaro, A. Castegna, The metabolic signature of macrophage responses, Front. Immunol. 10 (2019) 1462.
[56] J. Lichtnekert, T. Kawakami, W.C. Parks, J.S. Duffield, Changes in macrophage phenotype as the immune response evolves, Curr. Opin. Pharmacol. 13 (4) (2013) 555–564.
[57] K. Hamidzadeh, S.M. Christensen, E. Dalby, P. Chandrasekaran, D.M. Mosser, Macrophages and the recovery from acute and chronic inflammation, Annu. Rev. Physiol. 79 (2017) 567–592.
[58] M. Locati, G. Curtale, A. Mantovani, Diversity, mechanisms, and significance of macrophage plasticity, Annual review of pathology 15 (2020) 123–147.
[59] X. Wang, L. Fan, L. Cheng, Y. Sun, X. Wang, X. Zhong, Q. Shi, F. Gong, Y. Yang, Y. Ma, Z. Miao, Z. Zha, Biodegradable nickel disulfide nanozymes with GSH-depleting function for high-efficiency photothermal-catalytic antibacterial therapy, iScience 23 (7) (2020) 101281.